The Astrophysical Journal, 954:92 (15pp), 2023 September 1 https://doi.org/10.3847/1538-4357/ace899

Unpacking Merger Jets: A Bayesian Analysis of GW170817, GW190425 and Electromagnetic Observations of Short Gamma-Ray Bursts

Fergus Hayes[1], Ik Siong Heng[1], Gavin Lamb[2,3], En-Tzu Lin[4], John Veitch[1], and Michael J. Williams[1]
[1] SUPA, School of Physics and Astronomy, University of Glasgow, Glasgow, G12 8QQ, UK; fergus.hayes@glasgow.ac.uk
[2] Astrophysics Research Institute, Liverpool John Moores University, IC2 Liverpool Science Park, 146 Brownlow Hill, Liverpool, L3 5RF, UK
[3] School of Physics and Astronomy, University of Leicester, University Road, Leicester, LE1 7RH, UK
[4] Institute of Astronomy, National Tsing Hua University, Hsinchu 30013, Taiwan
Received 2023 May 3; revised 2023 June 26; accepted 2023 July 17; published 2023 August 25

Abstract

We present a novel fully Bayesian analysis to constrain short gamma-ray burst (sGRB) jet structures associated with cocoon, wide-angle, and simple top-hat jet models, as well as the binary neutron star (BNS) merger rate. These constraints are made given the distance and inclination information from GW170817, observed flux of GRB 170817A, observed rate of sGRBs detected by Swift, and the neutron star merger rate inferred from LIGO's first and second observing runs. A separate analysis is conducted where a fitted sGRB luminosity function is included to provide further constraints. The jet structure models are further constrained using the observation of GW190425, and we find that the assumption that it produced a GRB 170817–like sGRB which went undetected due to the jet geometry is consistent with previous observations. We find and quantify evidence for low-luminosity and wide-angle jet structuring in the sGRB population, independently from afterglow observations, with log Bayes factors of 0.45–0.55 for such models when compared to a classical top-hat jet. Slight evidence is found for a Gaussian jet structure model over all others when the fitted luminosity function is provided, producing log Bayes factors of $0.25–0.9 \pm 0.05$ when compared to the other models. However, without considering GW190425 or the fitted luminosity function, the evidence favors a cocoon-like model with log Bayes factors of 0.14 ± 0.05 over the Gaussian jet structure. We provide new constraints to the BNS merger rates of 1–1300 $\mathrm{Gpc^{-3}\,yr^{-1}}$ or 2–680 $\mathrm{Gpc^{-3}\,yr^{-1}}$ when a fitted luminosity function is assumed.

Unified Astronomy Thesaurus concepts: Gamma-ray bursts (629); Gravitational waves (678)

1. Introduction

The joint detection of both gravitational wave (GW) GW170817 (Abbott et al. 2017a), and counterpart short gamma-ray burst (sGRB) GRB 170817A (Goldstein et al. 2017; Savchenko et al. 2017), followed by the detection of kilonova AT 2017gfo (e.g., Evans et al. 2017; McCully et al. 2017) not only solidified the belief that many sGRBs are produced from the merger of binary neutron star (BNS) systems, but also began the era of GW multimessenger astronomy (Abbott et al. 2017d). The combination of both the electromagnetic (EM) and GW data gave insight into various problems that a detection through a single data channel could not provide, ranging from cosmology (Abbott et al. 2017c), the origin of the abundance of heavy elements in the Universe (Tanvir et al. 2017), tests of general relativity, and the speed of gravity (Abbott et al. 2017b) among others.

However the detection of the event not only provided answers but also provoked questions, as it was inferred through GW parameter inference that the event was exceptionally nearby at only 40 Mpc (Abbott et al. 2019), giving an observed isotropic luminosity of the event of 10^{47} erg $\mathrm{s^{-1}}$, three orders of magnitude lower than that observed for any other sGRB (Abbott et al. 2017b). It was also inferred through GW parameter inference that the event was viewed at a wide angle of 14°–41° from the central axis (Abbott et al. 2019). This led to the hypothesis that the jet of GRB 170817A exhibited some wide-angle structure to produce the observed flux, and that it may still have had a typically luminous central jet component. The long-duration observations of the event's afterglow across the EM spectrum provided further evidence for this claim (Troja et al. 2017, 2018a, 2020; Alexander et al. 2018; D'Avanzo et al. 2018; Lyman et al. 2018; Margutti et al. 2018; Mooley et al. 2018; Ruan et al. 2018).

While evidence for this wide-angle structure is provided by the multitude of afterglow observations, the functional form of the luminosity profile over viewing angle remains in question (e.g., Granot et al. 2017; Duffell et al. 2018; Gottlieb et al. 2018; Lamb & Kobayashi 2018; Mooley et al. 2018; Troja et al. 2018a; Beniamini et al. 2019; Fraija et al. 2019; Ioka & Nakamura 2019; Lamb et al. 2019, 2020; Salafia et al. 2019; Biscoveanu et al. 2020; Takahashi & Ioka 2021). Accurate modeling of this jet structure is important in both understanding the astrophysics of the event, and in preventing systematic biases in any multimessenger analysis that must make assumptions about the jet geometry (Lamb et al. 2021; Nakar & Piran 2021), which include constraints on BNS merger rate (Wanderman & Piran 2015), and the Hubble constant (Abbott et al. 2017c)—where it has been shown that without a reliable model of the jet structure the Hubble constant constraints are limited (Mastrogiovanni et al. 2021). An analogous observation to GRB 170817A and GW170817 was GRB 980425, which had a similar isotropic energy to GRB 170817A, and when considering the spectral peak energy of the prompt emission, it sits as an outlier from the Amati relation (Amati et al. 2002) for long GRBs (as does GRB 170817A for the equivalent relation for sGRBs). In the case of GRB 980425, the afterglow was not detected—there

was a supernova, SN1998bw, at both optical and radio (Galama et al. 1998; Kulkarni et al. 1998); at the time, this was claimed to be distinct from the cosmological GRB population.

With the promise of future GW BNS merger detections (Abbott et al. 2020b), a jet structure model that best represents the data of joint detection events should be discerned (Hayes et al. 2020). However, current analyses are limited to the data provided by GW170817/GRB 170817A (including AT 2017gfo), GW BNS merger event GW190425 (Abbott et al. 2020a), as well as the population of sGRBs detected independently of GW detection (Lien et al. 2016; Poolakkil et al. 2021). Previous similar work has considered constraining jet structure models with joint GW and EM detections using a Bayesian analysis (Biscoveanu et al. 2020; Farah et al. 2020; Hayes et al. 2020). The historical rate of detected sGRBs and GWs has also been used in Bayesian analyses to constrain the jet structure (Williams et al. 2018; Sarin et al. 2022). Work by Mogushi et al. (2019) and Tan & Yu (2020) combine the detection rates of sGRBs and GWs with the prompt emission data of GRB 170817A and the parameter inference results of GW170817, along with assuming a luminosity function fitted by short GRB events with known redshift. The jet structure has been constrained given the weak gamma-ray emission detected by the INTEGRAL SPI-ACS detector coincident with the GW event GW190425 in the work by Saleem et al. (2020). In this work, we put forward a comprehensive Bayesian framework that combines the prompt emission data from GRB 170817A, GW parameter inference posteriors of GW170817 and GW190425, GW-informed BNS merger rate, as well as the detection rate of sGRBs by the Neil Gehrels Swift Observatory (Swift) detector. This analysis is then further combined with the information provided by a luminosity function fitted by sGRB events with known redshifts to provide tighter constraints, with the caveat of also introducing bias into the analysis. We provide parameter constraints and model comparison results between a classical top-hat (TH) jet structure and three different jet structures with wide-angle structuring: a Gaussian, power-law, and double-Gaussian jet. These results are presented alongside constraints on the intrinsic luminosity (when it is not fitted by the luminosity function), and the merger rate for both cases.

The physical model assumed is detailed in Section 2, before the analysis method and data are laid out in Section 3. In Section 4 we report the results of the analysis, both for when the fitted luminosity function is incorporated and when it is not. In Section 5 the implications of the results are discussed and a conclusion provided in Section 6.

2. Background

The sGRB data consist of the observed T90 integrated flux F as well as the number of observed sGRBs $N_{\rm EM}$. The average T90 integrated flux $\hat{F}$ is related to the isotropic equivalent luminosity $L_{\rm iso}$ at a given viewing angle θ_v, as well as a redshift z-dependent luminosity distance d_L and k-correction k:

$$\hat{F} = \frac{L_{\rm iso}(\theta_v)}{4\pi d_L(z)^2 k(z)}. \tag{1}$$

The mean number of sGRBs $\hat{N}_{\rm EM}$ observed by a detector within a duration T that covers an area of sky equal to $\Delta\Omega$ depends on the redshift, viewing angle, and intrinsic luminosity $\Lambda = \{z, \theta_v, L_0\}$ through the number density:

$$\hat{N}_{\rm EM} = \int \frac{d\hat{N}_{\rm EM}}{d\Lambda}\left[\int p(D_{\rm EM}|\Lambda) dD_{\rm EM}\right] d\Lambda, \tag{2}$$

where $D_{\rm EM}$ denotes the selection effects of the detector, such that $D_{\rm EM} = 1$ if a detection is made and $D_{\rm EM} = 0$ otherwise.

We consider sGRBs detected by the Swift instrument, which has a detector response determined empirically in Lien et al. (2014) to fit

$$\int p(D_{\rm EM}|\Lambda) dD_{\rm EM} = \begin{cases} 0 & \text{if } \hat{F} < F_{\rm thr}, \\ a\frac{b + c\hat{F}/F_0}{1 + \hat{F}/dF_0} & \text{else}, \end{cases} \tag{3}$$

where $a = 0.47$, $b = -0.05$, $c = 1.46$, $d = 1.45$, $F_0 = 6 \times 10^{-6}$ erg s^{-1} cm^{-2}, and $F_{\rm thr} = 5.5 \times 10^{-9}$ erg s^{-1} cm^{-2}.

The relation between the number density and the physical parameters of Λ is

$$\frac{d\hat{N}_{\rm EM}}{d\Lambda} = T\frac{\Delta\Omega}{8\pi}\frac{\mathcal{R}_{\rm GRB}(z)}{1+z}\frac{dV(z)}{dz}p(L_0|\Sigma)\sin\theta_v, \tag{4}$$

where $V(z)$ is the co-moving volume, $\mathcal{R}_{\rm GRB}$ is the rate of sGRBs and $p(L_0|\Sigma)$ is the intrinsic luminosity function given the hyperparameter Σ.

2.1. Short Gamma-Ray Burst Rate

The rate of sGRBs is assumed to be in the form

$$\mathcal{R}_{\rm GRB}(z) = R_{\rm BNS} R_{\rm GRB}(z), \tag{5}$$

where $R_{\rm BNS}$ is the local rate of BNS mergers and $R_{\rm GRB}(z)$ is defined so that $R_{\rm GRB}(0) = 1$. This assumes that every BNS merger results in an sGRB, and that the number of sGRBs produced by neutron star–black hole mergers is negligible.

The form of $R_{\rm GRB}(z)$ can be assumed to follow the star formation rate $R_*(z)$ convolved with the probability distribution of the delay time between the system formation and the eventual merger that leads to the sGRB $P(t)$ (Wanderman & Piran 2015):

$$R_{\rm GRB}(z) \propto \int_{t_{\rm min}}^{T(\infty)-T(z)} \frac{R_*(z_*)}{1+z_*} P(t) dt, \tag{6}$$

where $z_* = z(T(z) + t)$ is the redshift when the system was formed, $T(z)$ is the *look-back time* and $t_{\rm min}$ is the minimum delay time. This minimum delay time is set to 20 Myr and $P(t) \propto 1/t$ according to Guetta & Piran (2006). The star formation rate is assumed to be of the form (Cole et al. 2001)

$$R_*(z) \propto \frac{a + bz}{1 + (z/c)^d} H(z), \tag{7}$$

where the parameter values are taken from Hopkins & Beacom (2006) to be $a = 0.017$, $b = 0.13$, $c = 3.3$, and $d = 5.3$.

2.2. Cosmology

A flat, vacuum-dominated Universe is assumed. The co-moving volume distribution over redshift is defined as

$$\frac{dV(z)}{dz} = 4\pi\frac{c}{H(z)}\left(\frac{d_L(z)}{1+z}\right)^2. \tag{8}$$

For a flat cosmology, the luminosity distance is related to the redshift by

$$d_L(z) = (1+z)\frac{c}{H_0}\int_0^z \frac{H_0}{H(z')}dz', \tag{9}$$

where H_0 is the Hubble constant and $H(z)$ is equal to

$$H(z) = H_0\sqrt{\Omega_m(1+z)^3 + \Omega_\Lambda}. \tag{10}$$

Here $\Omega_m = 0.308$ and $\Omega_\Lambda = 0.692$ are the matter density and dark energy density, respectively (Hogg 1999), with values taken from Adam et al. (2016) along with $H_0 = 67.8\ \mathrm{km\,s^{-1}\,Mpc^{-1}}$.

The look-back time, defined as the time between when a source emits light at redshift z and the time it is detected, is then

$$T(z) = \frac{1}{H_0}\int_0^z \frac{H_0}{(1+z')H(z')}dz'. \tag{11}$$

For a flat, vacuum-dominated Universe, the inverse function has an analytical expression (Petrillo et al. 2013)

$$z(T) = \left(\frac{\Omega_\Lambda}{\Omega_m}\right)^{1/3}\left[\left(\frac{1+W(T)}{1-W(T)}\right)^2 - 1\right]^{1/3} - 1, \tag{12}$$

where

$$W(T) = \exp\left[\ln\left(\frac{1+\sqrt{\Omega_\Lambda}}{1-\sqrt{\Omega_\Lambda}}\right) - 3H_0\sqrt{\Omega_\Lambda}T\right]. \tag{13}$$

The k-correction accounts for the cosmological redshifting in the intrinsic sGRB spectrum with respect to the detector's spectrum (Bloom et al. 2001):

$$k(z) = \frac{\int_{\nu_{s,1}/(1+z)}^{\nu_{s,2}/(1+z)} \nu f(\nu)d\nu}{\int_{\nu_1}^{\nu_2}\nu f(\nu)d\nu}, \tag{14}$$

where the source spectrum is bounded between $\nu_{s,1} = 1$ keV and $\nu_{s,2} = 10$ MeV. The energy range assumed for the Swift detector is $\nu_1 = 15$ keV and $\nu_2 = 150$ keV while $\nu_1 = 50$ keV and $\nu_2 = 300$ keV are assumed for the Fermi detector. Here we assume the form of $f(\nu)$ follows the Band function described in Band et al. (1993) with a peak spectral energy of 800 keV, and power-law indices of -1 and -2.25 for the low- and high-energy regimes, respectively. We note that while a comptonized spectral model is more often preferred for sGRBs (e.g., see Poolakkil et al. 2021), the peak spectral energy of sGRBs typically exceeds the high-energy limit of the Swift detector and therefore the model choice makes little impact.

2.3. Intrinsic and Isotropic Equivalent Luminosity

The luminosity structure of a gamma-ray burst is defined to be

$$L(\theta) = L_0 y_L(\theta), \tag{15}$$

where L_0 is the intrinsic luminosity at $\theta = 0$. It is assumed that the distribution of intrinsic luminosity L_0 follows a Schechter function:

$$p(L_0|\Sigma = \{L_0^*, \gamma\}) \propto \left(\frac{L_0}{L_0^*}\right)^{-\gamma} e^{-L_0/L_0^*}, \tag{16}$$

for $L_{\min} \leqslant L_0 \leqslant L_{\max}$, where $L_{\min} = 10^{-3}L_0^*$ and $L_{\max} = 10^2 L_0^*$.

Similarly, the Lorentz factor's dependence over angle follows

$$\Gamma(\theta) = (\Gamma_0 - 1)y_\Gamma(\theta) + 1, \tag{17}$$

with Γ_0 being the Lorentz factor of the jet at $\theta = 0$. Given these definitions, both y_L and y_Γ are defined to equal 1 at $\theta = 0$.

The Lorentz factor determines the degree of relativistic beaming, which for the luminosity is governed by

$$\mathcal{B}_L(\theta_v, \theta) = \frac{1}{4\Gamma(\theta)^6(A^2 - B^2)^2} \times \left(5\left(\frac{A}{\sqrt{A^2 - B^2}}\right)^3 + 3\left(\frac{A}{\sqrt{A^2 - B^2}}\right)\right), \tag{18}$$

with $A = 1 - \beta\cos\theta\cos\theta_v$ and $B = -\beta\sin\theta\sin\theta_v$ where $\beta = \sqrt{1 - \Gamma(\theta)^{-2}}$.

The apparent isotropic equivalent luminosity, for an observer at θ_v from the jet axis, can then be related to the intrinsic luminosity via the beaming function by combining Equation (15) and Equation (18):

$$L_{\mathrm{iso}}(\theta_v) = L_0\int_0^{\theta_j}\frac{1}{2}\mathcal{B}(\theta_v, \theta)y_L(\theta)\sin\theta d\theta, \tag{19}$$

where θ_j is the maximum angle for which the beaming of gamma-rays occurs. A conservative maximum outer jet angle for the emission of gamma-rays is approximated by considering scattering by electrons accompanying baryons within the jet. The condition is given by Matsumoto et al. (2019) and Lamb et al. (2022):

$$\Gamma(\theta_j) \simeq 19.1\left(\frac{L(\theta_j)}{10^{51}\ \mathrm{erg\ s^{-1}}}\right)^{1/6}, \tag{20}$$

Beyond this limit, $\theta > \theta_j$, the jet becomes opaque to gamma-rays.

2.4. Jet Structures

The implications of structuring within compact stellar merger jets for the EM counterparts from GW detected systems has been highlighted in the literature (Lazzati et al. 2017b; Lamb & Kobayashi 2017; Kathirgamaraju et al. 2018; Beniamini et al. 2020); here, we choose a sample of fiducial jet structure models that are representative of the literature diversity.

The TH jet is the simplest structure, where the beam is uniform until the jet opening angle θ_j where the jet sharply cuts off:

$$y_L(\theta) = \begin{cases} 1 & \text{if } 0 \leqslant \theta \leqslant \theta_j, \\ 0 & \text{else.} \end{cases}$$
$$y_\Gamma(\theta) = \begin{cases} 1 & \text{if } 0 \leqslant \theta \leqslant \theta_j, \\ 0 & \text{else.} \end{cases} \tag{21}$$

We note that the condition expressed in Equation (20) is not enforced for this case, as Γ_0 is above the Equation (20) limit at all points within the jet.

Wide-angle structure can be introduced with a Gaussian jet (GJ) structure, described by a single-width parameter θ_σ (e.g.,

Rossi et al. 2002, 2004; Zhang & Meszaros 2002; Kumar & Granot 2003):

$$y_L(\theta) = e^{-\frac{1}{2}\left(\frac{\theta}{\theta_\sigma}\right)^2}, \quad y_\Gamma(\theta) = e^{-\frac{1}{2}\left(\frac{\theta}{\theta_\sigma}\right)^2}. \tag{22}$$

An alternative to the Gaussian profile has the wide-angle emission expressed as a three-parameter power-law (PL) jet structure (e.g., Kumar & Granot 2003; Rossi et al. 2004; Zhang et al. 2004), where the jet can be described by some uniform core out to width θ_c, and then the intrinsic luminosity structure falls off at wide angles according to power s and the Lorentz factor with a:

$$y_L(\theta) = \begin{cases} 1 & \text{if } 0 \leqslant \theta \leqslant \theta_c, \\ \left(\frac{\theta}{\theta_c}\right)^{-s} & \text{else.} \end{cases}$$
$$y_\Gamma(\theta) = \begin{cases} 1 & \text{if } 0 \leqslant \theta \leqslant \theta_c, \\ \left(\frac{\theta}{\theta_c}\right)^{-a} & \text{else.} \end{cases} \tag{23}$$

Finally, let us consider a two-component, or double-Gaussian jet (DG), with emission from both an inner core described by a Gaussian structure of width $\theta_{\rm in}$ and an outer cocoon described by width $\theta_{\rm out}$ (Salafia et al. 2020):

$$y_L(\theta) = (1 - \mathcal{C})e^{-\frac{1}{2}\left(\frac{\theta}{\theta_{\rm in}}\right)^2} + \mathcal{C}e^{-\frac{1}{2}\left(\frac{\theta}{\theta_{\rm out}}\right)^2},$$
$$y_\Gamma(\theta) = \frac{(1 - \mathcal{C})e^{-\frac{1}{2}\left(\frac{\theta}{\theta_{\rm in}}\right)^2} + \mathcal{C}e^{-\frac{1}{2}\left(\frac{\theta}{\theta_{\rm out}}\right)^2}}{(1 - \frac{\mathcal{C}}{\mathcal{A}})e^{-\frac{1}{2}\left(\frac{\theta}{\theta_{\rm in}}\right)^2} + \frac{\mathcal{C}}{\mathcal{A}}e^{-\frac{1}{2}\left(\frac{\theta}{\theta_{\rm out}}\right)^2}}. \tag{24}$$

The luminosity of the outer cocoon is equal to $\mathcal{C}L_0$ and the Lorentz factor $\mathcal{A}(\Gamma_0 - 1) + 1$.

We do not consider hollow-cone jet structure models in our study (see, e.g., Nathanail et al. 2021; Takahashi & Ioka 2021); we expect that the combination of our intrinsic luminosity distribution (Equation (16)) and the beaming (Equation (19)) will wash out the effect of any hollow-cone structuring within the core. For this study, the structure outside of the jet's core is the critical component.

3. Bayesian Framework

Constraints are placed on model parameters λ of a model M when given data $\mathcal{D}$ in Bayesian data analysis by determining the posterior distribution using the *Bayes theorem*:

$$p(\lambda|\mathcal{D}, M) = \frac{\mathcal{L}(\mathcal{D}|\lambda)\pi(\lambda)}{p(\mathcal{D}|M)}, \tag{25}$$

where $\mathcal{L}$ is the likelihood, π is the prior, and the normalization term $p(\mathcal{D}|M)$ is the evidence. Consider comparing two models M_1 and M_2 when given data $\mathcal{D}$. In the context of Bayesian data analysis, the statistic used to compare two models is the *posterior odds*, defined as

$$\mathcal{O}_{12} = \frac{p(M_1|\mathcal{D})}{p(M_2|\mathcal{D})} = \frac{p(M_1)}{p(M_2)}\frac{p(\mathcal{D}|M_1)}{p(\mathcal{D}|M_2)}. \tag{26}$$

Normally we are interested in cases where the a priori probability of either model being correct is comparable, and therefore the posterior odds is dominated by the *Bayes factor*:

$$\mathcal{B}_{12} = \frac{p(\mathcal{D}|M_1)}{p(\mathcal{D}|M_2)}, \tag{27}$$

which quantifies the contribution to the posterior odds given by the data $\mathcal{D}$. A value of $\ln \mathcal{B}_{12} > 0$ favors M_1, while $\ln \mathcal{B}_{12} < 0$ favors M_2.

The analysis is performed by applying the model described in Section 2 with an assumed jet structure from Section 2.4 given both GW and sGRB prompt emission data.

Table 1 lists the notation used in the following section. The data can be split into that produced by a GW-triggered event, denoted with the subscript "GW," and that produced from an EM trigger, denoted with the subscript "EM." Figure 1 displays the relations between the observable variables that are represented by shaded nodes and the latent variables represented by clear nodes through the edges. The part of the network contained within the panel is dependent on each GW event, while those outside of the panel describe the population of events.

Table 1
Shorthand Notation of the GW and EM Data as Well as Sets of Parameters of Interest

Variable	Description
$x_{\rm GW}$	GW detector data
$F_{\rm GW}$	sGRB detector data
$N_{\rm GW}$	Number of detected GWs
$N_{\rm EM}$	Number of detected sGRBs
Σ	Luminosity function hyperparameters
$R_{\rm BNS}$	BNS merger rate
Θ	Jet structure parameters
Φ	$\{\theta_v, d_L\}$
L_0	Intrinsic on-axis luminosity

The data from the $N_{\rm GW}$ GW-triggered events consist of the GW strain $x_{\rm GW}$ and the flux of the counterpart $F_{\rm GW}$. The GW-triggered events may not necessarily require a counterpart to be considered for the analysis. If the sky localization of the source coincides with the sky coverage of GRB detectors then we can assume that it was not detected due to its distance and orientation to us. The current events that meet these criteria are both GW170817 with GRB 170817A as well as GW190425 and the nondetection of its counterpart, under the assumption that an sGRB was produced, given the Fermi detector covered 50% of the sky localization, INTEGRAL SPI-ACS had a near-complete sky coverage (Martin-Carillo et al. 2019), and Konus-Wind covered the entire sky (Hosseinzadeh et al. 2019).

The EM-triggered events are simply the number of sGRB detections that Swift made within a 9.8 yr operational period (after assuming a 78% duty cycle over a 12.6 yr observation (Mogushi et al. 2019)), $N_{\rm EM}$.

The likelihood can be decoupled into two terms, one of which considers GW-triggered events and the other EM-triggered:

$$\mathcal{L} = \mathcal{L}_{\rm EM}\mathcal{L}_{\rm GW}. \tag{28}$$

The likelihood of the EM-triggered events is a Poisson distribution with a mean given in Equation (2):

$$\mathcal{L}_{\rm EM} = \frac{\hat{N}_{\rm EM}(\Theta, R_{\rm BNS}, \Sigma)^{N_{\rm EM}} e^{-\hat{N}_{\rm EM}(\Theta, R_{\rm BNS}, \Sigma)}}{N_{\rm EM}!}. \tag{29}$$

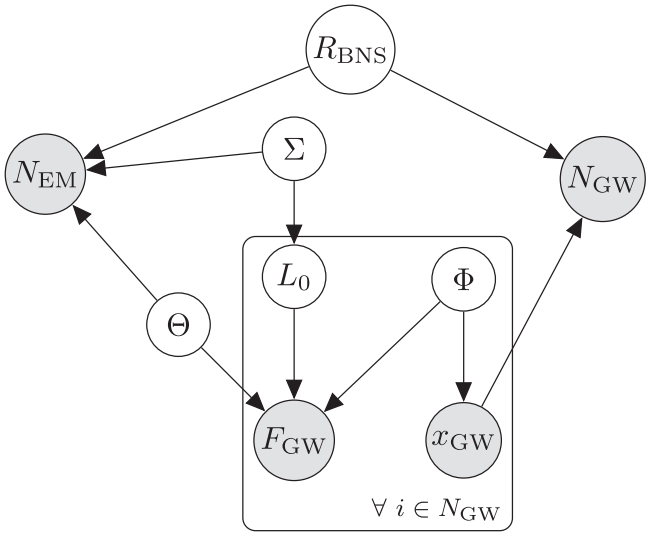

Figure 1. High-level Bayesian network of the model described in Section 2. The variable names are defined in Table 1.

The mean is evaluated over a regular grid of shape $(z, (2\theta/\pi)^{1/3}, \log_{10} L_0) = (\times 50, \times 100, \times 1000)$. The angular grid points were chosen to be distributed over a power law so as to populate low-θ areas of the parameter space with grid points, while also maintaining a relatively high density of points at wider angles where emission from some jet structures is still significant.

The GW-triggered events likelihood is the product of each of the $N_{\rm GW}$ events:

$$\mathcal{L}_{\rm GW} \propto \prod_{i=1}^{N_{\rm GW}} \sum_{j=1}^{S} p(F_{i,\rm GW}|\Theta, \Phi_{i,j}, L_{j,0}), \tag{30}$$

where S samples are taken of $\Phi_{i,j}$ and $L_{j,0}$ from $p(\Phi_i, L_0|x_{i,\rm GW}, \Sigma)$. The parameters can be sampled from separate distributions $p(\Phi_i|x_{i,\rm GW})$ and $p(L_0|\Sigma)$, respectively, where $p(\Phi_i|x_{i,\rm GW})$ are samples from the posteriors produced from GW parameter estimation for each event. The likelihood of the prompt emission of the GW-triggered events is assumed to be a Gaussian distribution of width σ_F about a mean described in Equation (1):

$$p(F_{\rm GW}|\Theta, \Phi, L_0) = \frac{1}{\sqrt{2\pi\sigma_F^2}} \exp\left(-\frac{(F_{\rm GW} - F)^2}{2\sigma_F^2}\right). \tag{31}$$

The priors for the model are specified in Table 3 for each of the GRB rate, luminosity function, and jet structure parameters. A normal distribution is denoted $\mathcal{N}(\mu, \sigma)$ with a mean of μ and standard deviation of σ, a uniform distribution as $\mathcal{U}(A, B)$ with lower bound of A and upper bound of B, a Gamma distribution and inverse Gamma distribution as $\Gamma(\alpha, \beta)$ and $\Gamma^{-1}(\alpha, \beta)$ with a shape of α and a scale of β (not to be confused with the Lorentz factor $\Gamma(\theta)$). We assume that every BNS merger results in a GRB so that $\epsilon_{\rm BNS} = 1$.

The T90 integrated flux of GRB 170817A in the Fermi detector's 50–300 keV band is set at $F_{170817} = 1.4 \times 10^{-7}$ erg s^{-1} cm^{-2} with an uncertainty of $\sigma_{170817} = 3.64 \times 10^{-8}$ erg s^{-1} cm^{-2} (Goldstein et al. 2017). For the unobserved counterpart of GW190425, it is assumed that the T90 integrated flux takes a value of zero with an uncertainty of $\sigma_{190425} = 10^{-8}$ erg s^{-1} cm^{-2} as a conservative upper bound to the Fermi detector's detection threshold (Tan & Yu 2020). We note that the detector sensitivity limit of INTEGRAL SPI-ACS approaches that of the Fermi detector, which had a more complete sky coverage in comparison. The distance and viewing angle posteriors of GW170817 and GW190425 are each represented by 500 samples taken from the their respective parameter estimation data releases. In this work we consider an observing period of approximately 9.8 yr by the Swift detector in which it observed $N_{\rm EM} = 107$ sGRBs as recorded by Lien et al. (2016), given a sky coverage of $\Delta\Omega = 0.1$. The log prior on the rate of BNS mergers of $\mathcal{N}(-6.6, 0.77)$ is roughly chosen to reflect the constraints imposed to the rates by GWTC-2 (Abbott et al. 2020c). The log prior on L_0^* is centered around the fitted value taken from Mogushi et al. (2019) with a standard deviation set to span one order of magnitude. This is chosen to reflect some prior information in the allowed luminosity from prior observations, but with a width to allow for flexibility into higher- or lower-luminosity regimes.

Table 2
Summary of the Data Used in the Analysis

Data set	Data
$\mathcal{D}_{170817}$	$\{x_{170817}, F_{170817}\}$
$\mathcal{D}_{190425}$	$\{x_{190425}, F_{190425}\}$
$\mathcal{D}_R$	$\{N_{\rm EM}, N_{\rm GW}\}$
$\mathcal{D}_{170817+R}$	$\{\mathcal{D}_{170817}, \mathcal{D}_R\}$
$\mathcal{D}_{\rm all}$	$\{\mathcal{D}_{170817}, \mathcal{D}_{190425}, \mathcal{D}_R\}$

Posteriors and Bayes factors are calculated from Equations (25) and (27) by assigning $\mathcal{D}$ and λ as the variables in Table 1. We collect the data into three sets: one only given the number of Swift detections $N_{\rm EM}$ and GW detections $N_{\rm GW}$ called $\mathcal{D}_R$, another with the combined GW170817 GW x_{170817} and EM data F_{170817} called $\mathcal{D}_{170817}$, and the other with GW190425 GW data x_{190425} and the flux from the nondetection F_{190425} called $\mathcal{D}_{190425}$. The analysis is performed on five combinations of these data sets as shown in Table 2: $\mathcal{D}_{170817} = \{x_{170817}, F_{170817}\}$, $\mathcal{D}_{190425} = \{x_{190425}, F_{190425}\}$, $\mathcal{D}_R = \{N_{\rm EM}, N_{\rm GW}\}$, $\mathcal{D}_{170817+R} = \{\mathcal{D}_{170817}, \mathcal{D}_R\}$, and $\mathcal{D}_{\rm all} = \{\mathcal{D}_{170817}, \mathcal{D}_{190425}, \mathcal{D}_R\}$. We allow that $\lambda = \{\Sigma, \mathcal{R}_0, \Theta_M\}$, where Θ_M are the jet structure model parameters dependent on jet structure model M. The three analyses are repeated for each of the jet structure models: $M =$ TH, GJ, PL, and DG.

The posterior samples and evidence for each case are calculated via the nested sampling algorithm NESSAI, which utilizes machine-learning techniques to drastically reduce the number of evaluations of the expensive likelihood function (Williams et al. 2021).

4. Results

The analysis that is described in the previous section is applied to all three sets of data. The full corner plots for each jet structure model are shown in the Appendix, where Figure A1 shows the results for the TH jet, Figure A2 the GJ, Figure A3 the PL jet and Figure A4 the DG jet structure model. The posteriors for each of the data sets are overlaid upon one another where $\mathcal{D}_{170817}$ is shown in red, $\mathcal{D}_{190425}$ in orange, $\mathcal{D}_R$ in violet, $\mathcal{D}_{170817+R}$ in blue, and $\mathcal{D}_{\rm all}$ in black. The log evidence $\ln p(\mathcal{D}|M)$ that corresponds to each posterior is shown in

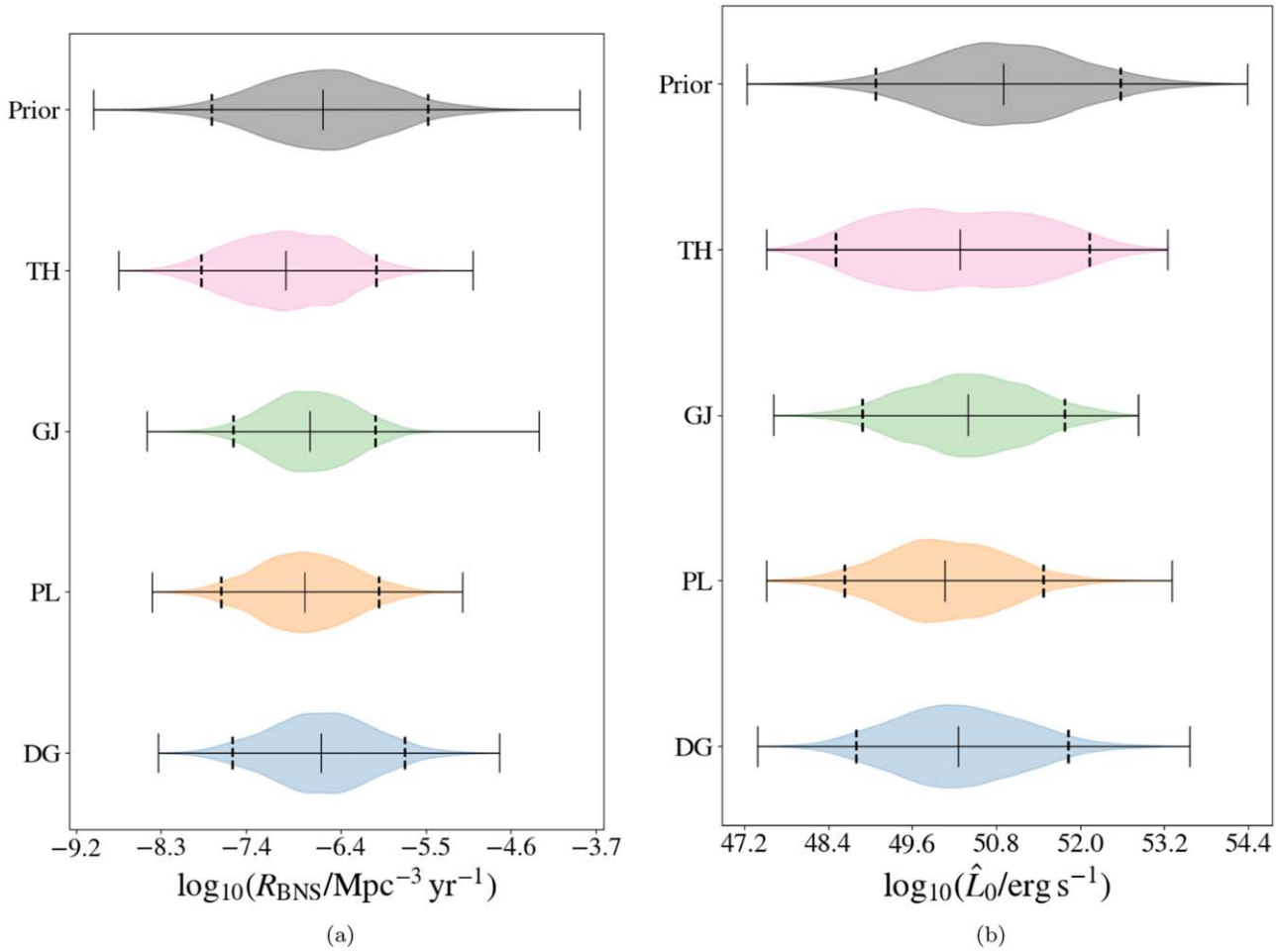

Figure 2. Posterior distributions of (a) the rate of binary neutron star (BNS) mergers and (b) the mean intrinsic luminosity $\hat{L}_0$ assuming the top-hat jet (TH, pink), Gaussian jet (GJ, green), power-law jet (PL, orange), and double-Gaussian jet (DG, blue) models when given $\mathcal{D}_{\rm all}$. The solid vertical lines represent the minimum and maximum of each distribution while the thickness of the fill in between represents the probability density. The dashed vertical lines represent 90% credible intervals. The median is shown by the middle solid line. The top distribution represents the prior distribution taken from Table 3 for $\log_{10} R_{\rm BNS}$, L_0 and γ, respectively. Similar posterior distributions are recovered for models with wide-angle structuring in comparison to the TH model case.

Table A1 for each of the five data sets over the four jet structure models. The log Bayes factors between the different models given the same data set can simply be calculated by taking the difference between entries of the same row.

Much of the discussion in this section concerns the posterior constraints when all of the data are considered $\mathcal{D} = \mathcal{D}_{\rm all}$; however, the outcomes given the other subsets are considered to explain these results and provide further insight.

The log Bayes factors between the jet structure models are given as the left-hand entries of Table 4 when given the $\mathcal{D}_{\rm all}$ data. A positive value indicates that the data support the model of the row while a negative value supports the column model. Evidently the TH model is less favourable than the models with wide-angle jet structuring, with Bayes factors of -0.54, -0.46, and -0.55 between it and the GJ, PL, and DG jet structures, respectively. The log Bayes factors between the PL, GJ, and DG is slight, with only insignificant evidence in favor of the GJ and DG model of log Bayes factors of less than 0.1, and negligibly small log Bayes factors between the two.

The constraints on the rate of BNS mergers when given $\mathcal{D}_{\rm all}$ are shown in Figure 2(a) for the four jet structure models. These constraints take the form of posterior distributions that are represented in the violin plots, where the outermost solid vertical lines indicate the minimum and maximum sample value while the fill in between represents the probability density. The 90% narrowest credible intervals are shown by the vertical dashed lines which enclose the median indicated by the middle solid line. The posterior distributions are compared to samples from the prior distribution at the top of the figure. For all cases, the posterior places tighter constraints on the merger rate than the prior distribution. The cases with wide-angle structuring (GJ, Pl, and DG models) produce similar posterior distributions to one another, centered around a value of $\sim 10^{-7}$ Mpc^{-3} yr^{-1} consistent with the mean of the prior. The GJ structure produces the narrowest constraints with a 90% credible interval of $\log_{10} R_{\rm BNS}/{\rm Mpc}^{-3}\,{\rm yr}^{-1} = -6.7^{+0.7}_{-0.8}$, compared to the PL and DG models of $-6.8^{+0.7}_{-0.9}$ and $-6.6^{+0.9}_{-0.9}$, respectively. The TH model favors lower rates of BNS mergers, and even pushes the lower bound on the 90% credible interval to lower values of that of the prior, constraining it between $\log_{10} R_{\rm BNS}/{\rm Mpc}^{-3}\,{\rm yr}^{-1} = -7^{+0.9}_{-1.0}$.

The median intrinsic luminosity posteriors determined for each model when given $\mathcal{D}_{\rm all}$ is shown in Figure 2(b). The mean intrinsic luminosity $\hat{L}_0$ is determined by drawing L_0 and γ from the respective posterior distribution and then drawing 1000 samples from the corresponding Schechter function of Equation (16) before finding the ensemble median. This process is then repeated for 2000 median intrinsic luminosity

Table 3
Assumed Prior Distributions for Each Parameter

Model	Parameter	Prior
	$\log_{10} R_{\rm BNS}{}'$	$\mathcal{N}(-6.6, 0.77)$
	$\log_{10} L_0^{*\prime}$	$\mathcal{N}(51.6, 1)$
	γ	$\mathcal{U}(0, 1)$
	Γ_0	$\Gamma^{-1}(2, 2.5 \times 10^{-3})$
TH	θ_j	$\mathcal{U}(0, \pi/2)$
GJ	θ_σ	$\mathcal{U}(0, \pi/2)$
PL	θ_c	$\mathcal{U}(0, \pi/2)$
	s	$\Gamma(2, 4)$
	a	$\Gamma(2, 1)$
DG	$\theta_{\rm in}$	$\mathcal{U}(0, \pi/2)$
	$\theta_{\rm out}$	$\mathcal{U}(0, \theta_{\rm out})$
	$\log_{10} \mathcal{C}$	$\mathcal{U}(-6, 0)$
	$\log_{10} \mathcal{A}$	$\mathcal{U}(-6, 0)$

Notes. The analysis assumes one jet structure out of the top-hat (TH), Gaussian (GJ), power-law (PL), and double-Gaussian (DG) models. Some parameters are made unit-less so that $R_{\rm BNS}{}' = R_{\rm BNS}/{\rm Mpc}^{-3}\,{\rm yr}^{-1}$ and $L_0{}^{*\prime} = L_0^*/{\rm erg\ s}^{-1}$.

samples. These posteriors take a form similar to the rates posteriors in Figure 2 as violin plots where the shaded probability density is contained within the outermost maximum and minimum values indicated by the solid vertical lines, while the median is marked by the middle solid line. The median is enclosed by the narrowest 90% credible intervals displayed as dashed vertical lines. A distribution of prior samples of $\hat{L}_0$ is also plotted at the top of the figure, which is determined by sampling from the individual $\log_{10} L_0^*$ and γ priors defined in Table 3. The TH jet structure resembles the prior in width, but shifts to favor lower luminosity and exhibits some bimodality as the probability density pinches at the median. This is due to the bimodality of the L_0 posterior distribution in Figure A1 given $\mathcal{D}_{170817+R}$, which shall be discussed later in Section 5. The models with wide-angle structure tend toward lower mean intrinsic luminosity values, with the GJ model constrained to $\log_{10} \hat{L}_0/{\rm erg\ s}^{-1} = 50.4^{+1.6}_{-1.3}$, PL model $50.1^{+1.3}_{-1.6}$, and DG model of $50.2^{+1.5}_{-1.5}$. The TH model is constrained to $\log_{10} \hat{L}_0/{\rm erg\ s}^{-1} = 50.2^{+1.7}_{-1.7}$ which we can compare to the prior of $51^{+1.8}_{-1.8}$.

The constraints from the posteriors on the jet structure parameters given each jet structure model are shown in Table 5. The median is quoted along with the upper and lower bounds placed by the 90% narrowest credible intervals.

4.1. Fitted Luminosity Function

The analysis is repeated but instead of assuming a prior distribution on the luminosity scale and shape, a luminosity function (LF) is fitted from the observed isotropic equivalent luminosity of sGRBs with associated redshifts. The values of L_0 and γ are taken from the mean fitted Schechter function in Mogushi et al. (2019) of $\log_{10} L_0/{\rm erg\ s}^{-1} = 51.6$ and $\gamma = 0.55$, fitted to the isotropic equivalent luminosity of 35 sGRBs.

The log evidence between each of the jet structure models and the different data sets are shown in Table A2, while the respective Bayes factors when given $\mathcal{D}_{\rm all}$ between each of the jet structure models are shown on the right-hand entries of Table 4.

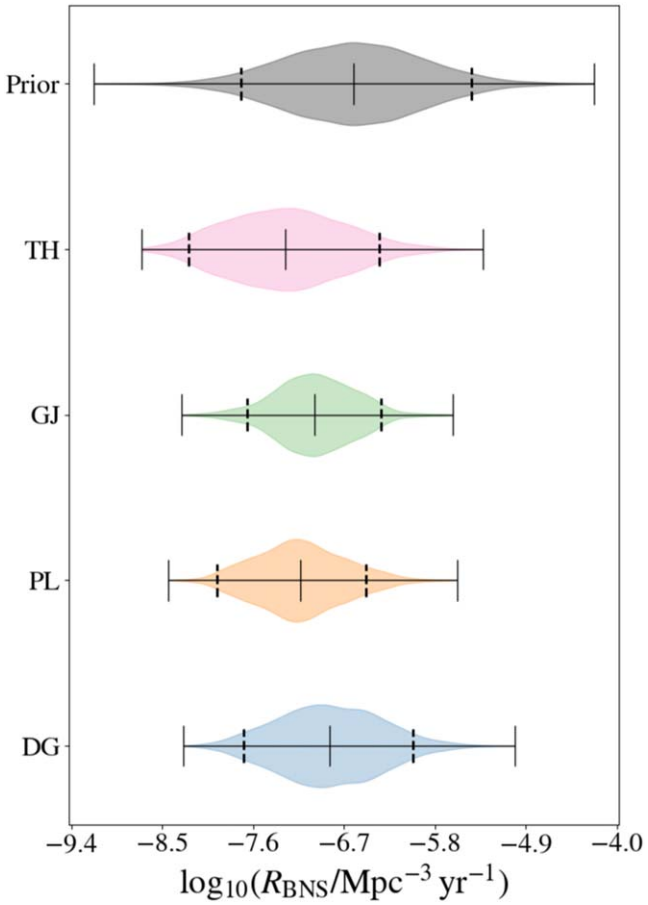

Figure 3. Posterior distributions of the rate of BNS mergers assuming the TH jet (pink), GJ (green), PL jet (orange), and DG jet (blue) models when given $\mathcal{D}_{\rm all}$ and the fitted luminosity function. The solid vertical lines represent the minimum and maximum of each distribution while the thickness of the fill in between represents the probability density. The dashed vertical lines represent 90% credible intervals. The median is shown by the middle solid line. The posterior distributions are compared to samples from the prior of $\mathcal{N}(-6.6, 0.77)$ at the top. All models recover similar constraints that narrow about the mean value assigned to the prior.

The posteriors on the local rate of BNS merger when given the fitted LF and $\mathcal{D}_{\rm all}$ are shown in Figure 3 in the same format as Figure 2(a) where the widths of the violin plots indicate the probability density, the maximum and minimum sample is indicated by the extreme solid vertical lines, and median with the middle solid vertical line. The narrowest 90% credible intervals are indicated by the dashed vertical lines and are $\log_{10} R_{\rm BNS}/{\rm Mpc}^{-3}\,{\rm yr}^{-1} = -7.0^{+0.7}_{-0.6}$, $-7.2^{+0.7}_{-0.8}$, $-6.8^{+0.8}_{-0.9}$ for the GJ, PL, and DG models, respectively. For the TH jet model, the rate is constrained to $\log_{10} R_{\rm BNS}/{\rm Mpc}^{-3}\,{\rm yr}^{-1} = -7.3^{+1.0}_{-0.9}$.

The constraints on the jet structure models given the fitted LF and $\mathcal{D}_{\rm all}$ are presented in Table 5 for each jet structure model, with the upper and lower bounds representing the narrowest 90% credible intervals.

5. Discussion

5.1. Wide-angle Jet Structuring

The log Bayes factors are greater than 0.45 for all models with wide-angle jet structure when compared to the TH model.

Table 4
The Log Bayes Factor $\ln \mathcal{B}$ between Each Model When Given $\mathcal{D}_{\rm all}$ without or with the Fitted Luminosity Function

$\ln \mathcal{B}_{\rm row,col}$	Top-hat	Gaussian	Power Law	Double Gaussian
Top-hat	0	−0.54/−0.91	−0.46/−0.45	−0.55/−0.64
Gaussian	0.54/0.91	0	0.08/0.46	−0.01/0.27
Power law	0.46/0.45	−0.08/−0.46	0	−0.09/−0.19
Double Gaussian	0.55/0.64	0.01/−0.27	0.09/0.19	0

Notes. A positive value is evidence toward the model of the row while a negative is evidence that favors the column model. Slight evidence is provided for models with wide-angle structuring over the TH model while little evidence distinguishes between the PL, GJ, and DG models without the fitted luminosity function. When the fitted luminosity function is included, slight evidence is further provided in favor of the GJ over the DG and PL jet structures while the TH remains least favored. All values can be assumed to have uncertainties of ±0.05.

Table 5
Constraints Placed on Each of the Variables for Each Model Given Data Set $\mathcal{D}_{\rm all}$ with and without the Fitted Luminosity Function

Model	Parameter	Constraints	
		w/o Fitted LF	Fitted LF
TH	θ_j	$14.9^{+46.0\circ}_{-14.3}$	$9.2^{+17.1\circ}_{-7.9}$
GJ	θ_σ	$5.9^{+28.2\circ}_{-5.4}$	$4.2^{+5.2\circ}_{-3.2}$
PL	θ_c	$10.6^{+32.9\circ}_{-10.0}$	$6.0^{+9.2\circ}_{-4.9}$
	s	$6.7^{+8.1}_{-5.2}$	$6.4^{+7.9}_{-4.3}$
	a	$1.5^{+2.2}_{-1.4}$	$1.5^{+2.1}_{-1.4}$
DG	$\theta_{\rm in}$	$6.3^{+24.1\circ}_{-6.2}$	$3.6^{+6.2\circ}_{-2.8}$
	$\theta_{\rm out}$	$49.3^{+40.7\circ}_{-38.0}$	$46.2^{+43.1\circ}_{-36.3}$
	$\log_{10}\mathcal{C}$	$-3.8^{+2.9}_{-2.2}$	$-4.1^{+1.9}_{-1.9}$
	$\log_{10}\mathcal{A}$	$-3.0^{+2.8}_{-2.9}$	$-3.1^{+2.9}_{-2.7}$

Note. The median of each posterior distribution is quoted along with upper and lower bounds placed by 90% credible intervals.

This is due to the TH jets failing to resolve the number of observed sGRBs with the flux of GRB 170817A when assuming that the event had a typical event opening angle. Given the assumed star formation rate and the constraints on the BNS merger rate from GW detections, to obtain a Swift sGRB detection rate of 11 $\rm yr^{-1}$, the jets are either predicted to have narrow opening angles and high luminosities or wide opening angles and low luminosities. This constraint can be seen in the bottom left corner plot panel of Figure A1 in the violet posterior, where much of the probability density is concentrated in the low luminosity and wide opening angle area of the parameter space. In contrast, the constraints made by GW170817 and GRB 170817A favor a wide opening angle of $\theta_j \lesssim \theta_v$ and a high-luminosity event, as seen in the bottom left-hand panel of Figure A1 in the red posterior. This is because emission from an event with a TH jet structure when viewed at a wide angle can only come from Doppler beaming, which falls off very sharply with increased viewing angles. As $\theta_v > \theta_j$ is more probable than $\theta_v \gtrsim \theta_j$, then a high-luminosity event is deemed more probable. The two constraints produce posteriors that share very little overlap in the parameter space, leading to the TH model providing a smaller evidence than the other models. This contradiction also manifests in the bimodality of the mean luminosity posterior for the TH jet model, as seen in Figure 2(b), as the lower-luminosity, high-density region corresponds to the constraint produced from the observed number of GRBs, while the higher-luminosity, high-density region corresponds to the constraints made by GW170817 and GRB 170817A.

Jet structure models with wide-angle structuring are only favored when the data from GW170817/GRB 170817A of $\mathcal{D}_{170817}$ are combined with the event rate information from $\mathcal{D}_R$. When these data sets are considered individually the evidence for a TH jet structure is comparable to or higher than the other models in most cases, as seen in the Table A1. The inclusion of the GW190425 event provides evidence against jets with wide-angle structuring. This can be seen by comparing the difference in log evidence between the TH jet and the other models given $\mathcal{D}_{170817+R}$, and the difference when given $\mathcal{D}_{\rm all}$, where there is relatively less evidence between the models when $\mathcal{D}_{190425}$ is included. As it is assumed that GW190425 produced a counterpart that went undetected due to its distance and viewing angle, the event places an upper bound on the luminosity and jet width. This upper bound on the jet structure limits the possible wide-angle emission, which makes wide-angle jet structuring unnecessary to explain the event.

5.2. Cocoon Emission

The existence of cocoon emission and its contribution to the jet energy of sGRBs has been a subject of interest both before and after the detection of GRB 170817A (Nakar & Piran 2016; Lazzati et al. 2017a, 2017b; Kasliwal et al. 2017; Bromberg et al. 2018; Margutti et al. 2018; Mooley et al. 2018). The DG jet structure provides a stand-in for a jet structure with cocoon-like emission, where the outer Gaussian provides a secondary component for the emission contribution from an energetic cocoon. Interestingly, comparing the log evidence given the DG jet model to the other models shows weak evidence for the DG jet structure when considering $\mathcal{D}_{170817}$, $\mathcal{D}_R$, $\mathcal{D}_{170817+R}$ for all cases (with the exception of $\ln p(\mathcal{D}_{170817+R}|\rm GJ)$ given the fitted Schechter luminosity function), suggesting it is the favourable model when considering both GW170817/GRB 170817A and the observed rate data. As discussed in the previous section, GW190425 places an upper bound on the wide-angle emission and provides support for the TH and PL jet structure with sharper cut-offs. Given that the suitability of GW190425 in the analysis is not as clear-cut as an event like GW170817 due to the uncertainty of the EM coverage of the event, this result should not be disregarded. While this may not provide convincing evidence for the observation of cocoon emission, it suggests that, with the inclusion of future events, the necessity for the cocoon-like component can be better

assessed and improve our understanding of sGRB physics such as the jet launch time (Zhang 2019), provide insight into the jet launching mechanism, and answer longstanding questions about kilonovae such as the abundance of early ultraviolet emission of AT 2017gfo (for a review, see Burns 2020).

5.3. Rate of Binary Neutron Star Mergers

The narrowest 90% credible intervals of the rate of BNS mergers are constrained within 1–1300 $\mathrm{Gpc^{-3}\,yr^{-1}}$ independent of the jet structure model considered, improving upon the constraints imposed by GWTC-3 (Abbott et al. 2023). The rate is further constrained to the interval of 2–680 $\mathrm{Gpc^{-3}\,yr^{-1}}$ when the fitted Schechter LF is assumed. These constraints favor lower merger rates than constraints placed by other comparable analyses performed before GWTC-3 (e.g., see for a comparison Escorial et al. 2022). Future BNS detections will provide tighter constraints on their merger rate. These constraints will allow for a tighter prior to be placed on the rate of mergers, allowing the possible jet structures to be distinguished.

5.4. Luminosity Function

Two different cases are explored in the analysis: one where the LF is fitted in advance of the analysis, and the other where priors are placed on the LF parameters L_0^* and γ. When priors are placed on the LF, the luminosity function generally favors low luminosities for all models assumed. This is apparent in Figure 2(b) where the $\hat{L}_0$ posterior for all jet structure models shifts to low luminosity when compared to the prior distribution, and mean values of $\log_{10}(L_0^*/\mathrm{erg\ s^{-1}})$ shift to 51–51.25 in comparison to the value of 51.6 taken from Mogushi et al. (2019) and used as the mean of the prior.

The inclusion of the fitted LF informs the analysis of the prompt emission of all sGRBs that are used in the fit—information that is excluded from the case where the luminosity priors are placed. This allows for narrower constraints on the jet structure model parameters, as seen by comparing the left- to right-hand side of the last column of Table 5. Similarly, this also leads to tighter constraints in the BNS merger rate posteriors as seen by comparing Figure 2(a) to Figure 3. Interestingly, fitting the LF provides slight evidence for the GJ structure model over all other jet structures given all the data, as seen by the right-hand log Bayes factors shown in Table 4. However, fitting the LF requires assumptions about the jet structure to be made, which will lead to biases in this analysis. In Mogushi et al. (2019), which the fitted LF is taken from, the fit is produced by assuming that all 35 sGRB prompt emission observations with associated redshifts are seen on-axis. However, if some of the events used in fitting the LF were observed at an angle, then the observed variability in their observed isotropic luminosity would be wrongly attributed to variability in the intrinsic luminosity. Assuming a wider distribution to the intrinsic luminosity would favor wider jet structures. To avoid this bias, a future analysis should adjust the likelihood to accommodate the flux data of all observed sGRBs along with their associated redshifts while placing priors on the LF parameters. This would allow for the LF to be fitted internally within the analysis without having to make the additional jet structure assumptions in a pre-processing step.

5.5. GW190425

The inclusion of GW190425 in the analysis provides an upper bound to the wide-angle jet structure emission, due to the absence of an EM detection. The viewing angle posterior of the event exhibits a similar distribution as that of GW170817, while the distance to the event is notably larger at a distance of approximately 160 Mpc compared to GW170817's distance of 40 Mpc. The event is close enough in proximity that, if observed on-axis and is of typical luminosity, would produce a flux tens or hundreds of times greater than GRB 170817A. However, there are assumptions about the event that are made by including it in this way. First, it implies that the event produced an sGRB. This assumption is made explicitly in the analysis when incorporating the observed rate of merger, where every BNS merger is assumed to produce an sGRB in Equation (5). However, as the prior on the local rate of BNS mergers is relatively wide and covers multiple orders of magnitude, this assumption should not affect the analysis when considering the whole population as long as BNS mergers do typically produce sGRBs. This assumption has a much greater impact when analyzing individual events where wrongly asserting a particular event produced an sGRB leads to false conclusions. Second, it is assumed that the event would be observed given a wider jet structure or higher luminosity. While the event was within the field of view of the Konus-Wind satellite, the incomplete sky coverage of the event by the more sensitive detectors such as the Fermi-GBM detector and Swift-BAT brings the detectability of the event into question. Despite the validity of these assumptions, and that the event produces evidence against wide-angle jet structuring, it is found that GW190425 is still compatible with the jet structure models given the rest of the data. This can be assessed by the comparison of $\ln p(\mathcal{D}_{\rm all}|M)$ to $\ln p(\mathcal{D}_{190425}|M) + \ln p(\mathcal{D}_{170817+R}|M)$ for each of the jet structure models M. For all models, the value of $\ln p(\mathcal{D}_{\rm all}|M) > p(\mathcal{D}_{190425}|M) + \ln p(\mathcal{D}_{170817+R}|M)$, suggesting that the observation of GW190425 is informative to the analysis in all cases, and does not conflict with the constraints imposed to the model given by the detection of GW170817/GRB 170817A and the rate of observed sGRBs. This result suggests that it is feasible for GW190425 to have had a typical sGRB counterpart with the same jet structure as GRB 170817A that would have remained undetectable to our instrumentation even given full sky coverage. This observation is consistent with the result obtained in Saleem et al. (2020) where it was concluded that such a structured jet is consistent with the observed flux of the INTEGRAL SPI-ACS detector given the detector's flux upper limit.

6. Conclusion

We provide an extensive Bayesian analysis that constrains the jet structure, intrinsic LF, and rate of BNS mergers as well as providing a comparison between competing jet structure models. This is achieved by combining four data avenues: (1) the parameter inference posteriors from a GW trigger, (2) the sGRB flux when a counterpart is detected or the detector flux upper limit otherwise, (3) the observation rate of detected sGRBs, and (4) the merger rate informed from GW observations. We perform this analysis using the GW triggers GW170817 and GW190425, GRB 170817A, the nondetection of a GW190425 counterpart, the rate of sGRB detections by the

Swift detector within a 9.8 yr observation period, and a merger rate consistent with the constraints imposed by GWTC-2 (Abbott et al. 2020c). This provides us with the following results:

1. The rate of BNS mergers is constrained within 1–1300 $\mathrm{Gpc}^{-3}\,\mathrm{yr}^{-1}$, improving upon the results of GWTC-3.
2. Wide-angled jet structures prove more compatible with the given model than TH jet in explaining the observed number of sGRBs in the wake of the low observed isotropic luminosity of GRB 170817A.
3. Slight evidence is provided for a cocoon-like wide-angle jet structure when considering the observed rate of sGRBs and GRB 170817A. However, the evidence becomes awash across all wide-angle jet structures when GW190425 is included in the analysis.
4. While providing evidence against wide-angle structuring, the hypothesis that GW190425 had a typical sGRB counterpart with a GRB 170817A–like jet structure and would remain undetectable to the Fermi detector given full-sky coverage is feasible given the model.

The analysis was extended to consider a fitted intrinsic LF to further incorporate the detected flux and estimated redshifts of past sGRB detections. This provides the following results:

1. The rate of BNS mergers is further constrained to 2–680 $\mathrm{Gpc}^{-3}\,\mathrm{yr}^{-1}$.
2. Slight evidence for the GJ structure is provided, unless GW190425 is excluded in which the cocoon-like DG jet structure is equally favored.

However, we note that the fitting of the LF requires strong assumptions about the jet structure and therefore introduces a bias toward jet structures with wide central components. Interestingly, this bias does not appear to manifest in the resulting Bayes factors where the TH jet loses favor over the wide-angle jet structures. A future analysis will work to incorporate the flux measurements and inferred redshifts of detected sGRBs directly, and therefore avoid introducing this bias. Future work would also include incorporating afterglow data into the analysis for events that coincide with a GW detection (Lin et al. 2021), as well as additional very long baseline interferometry (VLBI) imaging data for GW170817 (Ghirlanda et al. 2019) or when VLBI data are available for future events, where the simple analytic method used to approximate the inclination angle from superluminal motion has been shown to be reasonably accurate (Fernández et al. 2022). Additionally, the short GRB population includes claims of "off-axis" events such as GRB 150101B (Troja et al. 2018b), an under-luminous GRB; here the inclusion of afterglow data in any future analysis could improve the marginal structured jet preference found via the current analysis which considers only the prompt emission and redshift.

Acknowledgments

We are grateful for computational resources provided by Cardiff University, and funded by an STFC (grant No. ST/I006285/1) supporting UK Involvement in the Operation of Advanced LIGO. The authors thank Shiho Kobayashi for fruitful discussions. F.H. was supported by Science and Technology Research Council (STFC) (grant No. ST/N504075/1). J.V., I.S.H. and M.J.W. are supported by STFC (grant No. ST/V005634/1). M.J.W. was also supported by STFC (grant No. 2285031). G.P.L. is supported by a Royal Society Dorothy Hodgkin Fellowship (grant Nos. DHF-R1-221175 and DHFERE-221005). E.T.L is supported by National Science and Technology Council (NSTC) of Taiwan (grant No. 111-2112-M-007-020).

Code Availability

http://github.com/Fergus-Hayes/Unpacking_the_jet

Appendix A
Evidences

The log evidence for each data set given each model is provided in Table A1 while Table A2 provides the evidence for when the fitted luminosity function is assumed.

Table A1
Log Evidence $\ln p(\mathcal{D}|M)$ Given the Five Different Data Sets When Assuming Each of the Four Models

Data $\mathcal{D}$	Model M			
	Top Hat	Gaussian	Power Law	Double Gaussian
$\mathcal{D}_{170817}$	11.87 ± 0.02	11.8 ± 0.03	11.79 ± 0.03	12.08 ± 0.03
$\mathcal{D}_{190425}$	17.29 ± 0.01	16.3 ± 0.03	16.41 ± 0.02	16.42 ± 0.03
$\mathcal{D}_{R}$	-7.67 ± 0.04	-7.8 ± 0.04	-7.73 ± 0.04	-7.53 ± 0.04
$\mathcal{D}_{170817+R}$	4.45 ± 0.05	5.23 ± 0.05	5.15 ± 0.05	5.37 ± 0.05
$\mathcal{D}_{\mathrm{all}}$	22.12 ± 0.05	22.66 ± 0.05	22.58 ± 0.05	22.67 ± 0.05

Table A2
Log Evidence $\ln p(\mathcal{D}|M)$ Given the Five Different Data Sets When Assuming Each of the Four Models Given the Fitted Schechter LF

Data $\mathcal{D}$	Model M			
	Top Hat	Gaussian	Power Law	Double Gaussian
$\mathcal{D}_{170817}$	11.48 ± 0.02	11.6 ± 0.03	11.45 ± 0.03	11.62 ± 0.03
$\mathcal{D}_{190425}$	17.28 ± 0.01	16.23 ± 0.03	16.29 ± 0.03	16.21 ± 0.03
$\mathcal{D}_{R}$	-8.08 ± 0.05	-8.53 ± 0.05	-8.23 ± 0.05	-7.84 ± 0.05
$\mathcal{D}_{170817+R}$	3.86 ± 0.05	4.97 ± 0.05	4.74 ± 0.05	4.91 ± 0.05
$\mathcal{D}_{\mathrm{all}}$	21.87 ± 0.05	22.78 ± 0.05	22.32 ± 0.05	22.51 ± 0.05

Appendix B
Posteriors

The full posteriors are shown in overlaid corner plots given all data sets in Figures A1, A2, A3, and A4 for the TH, GJ, PL and DG jet structure models, respectively.

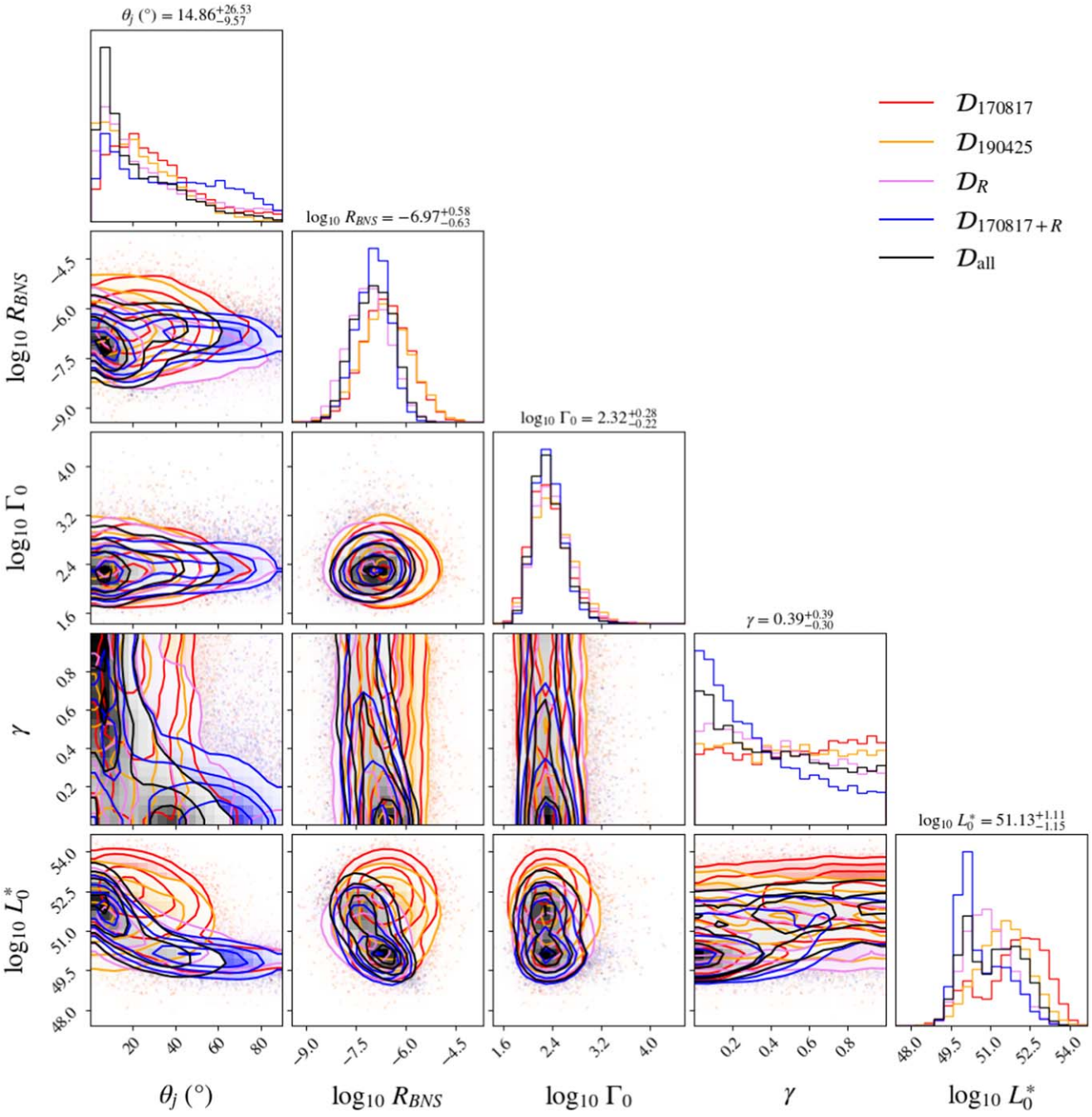

Figure A1. Parameter posterior for all data subsets given the TH jet structure model.

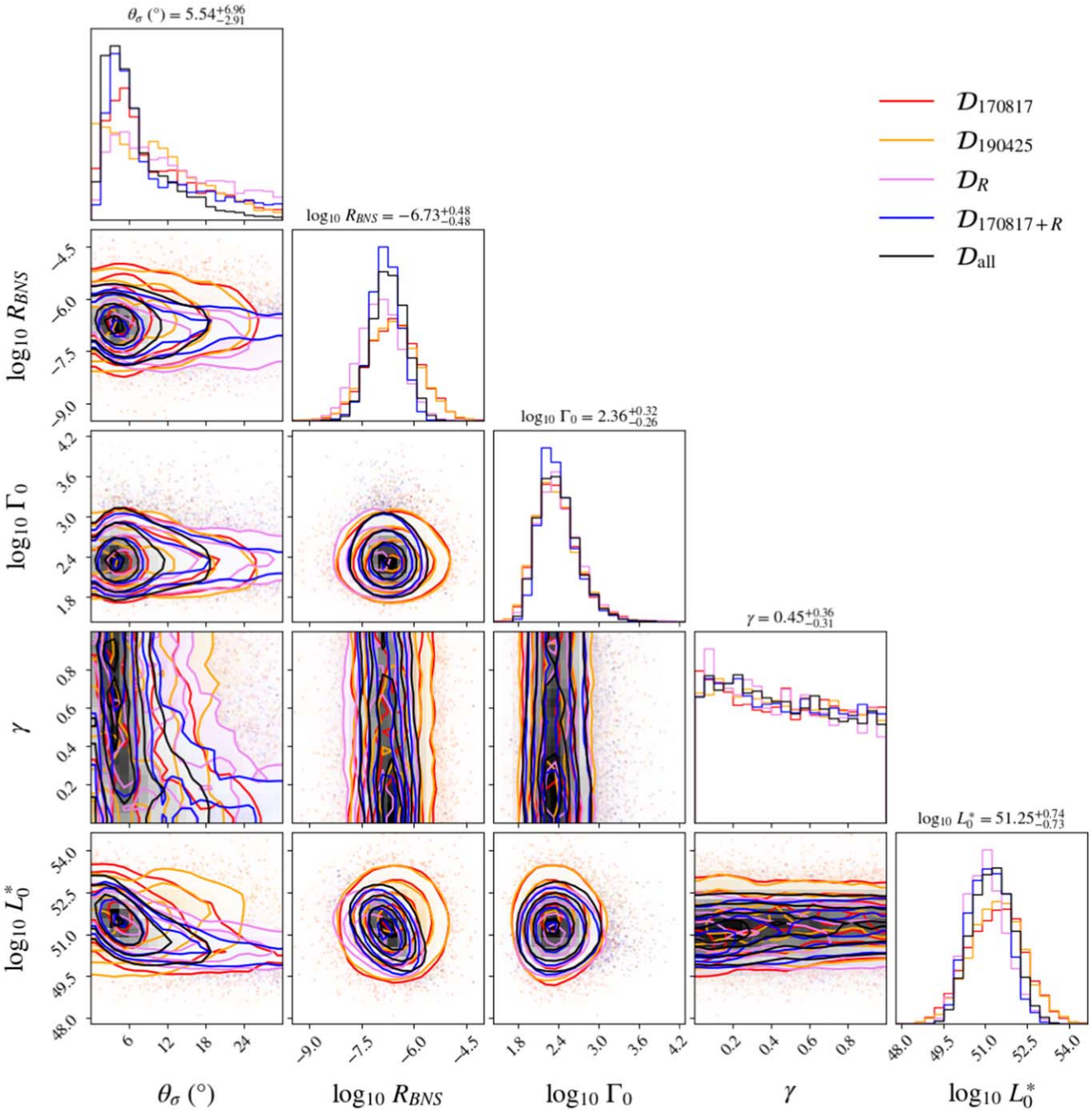

Figure A2. Parameter posterior for all data subsets given the GJ structure model.

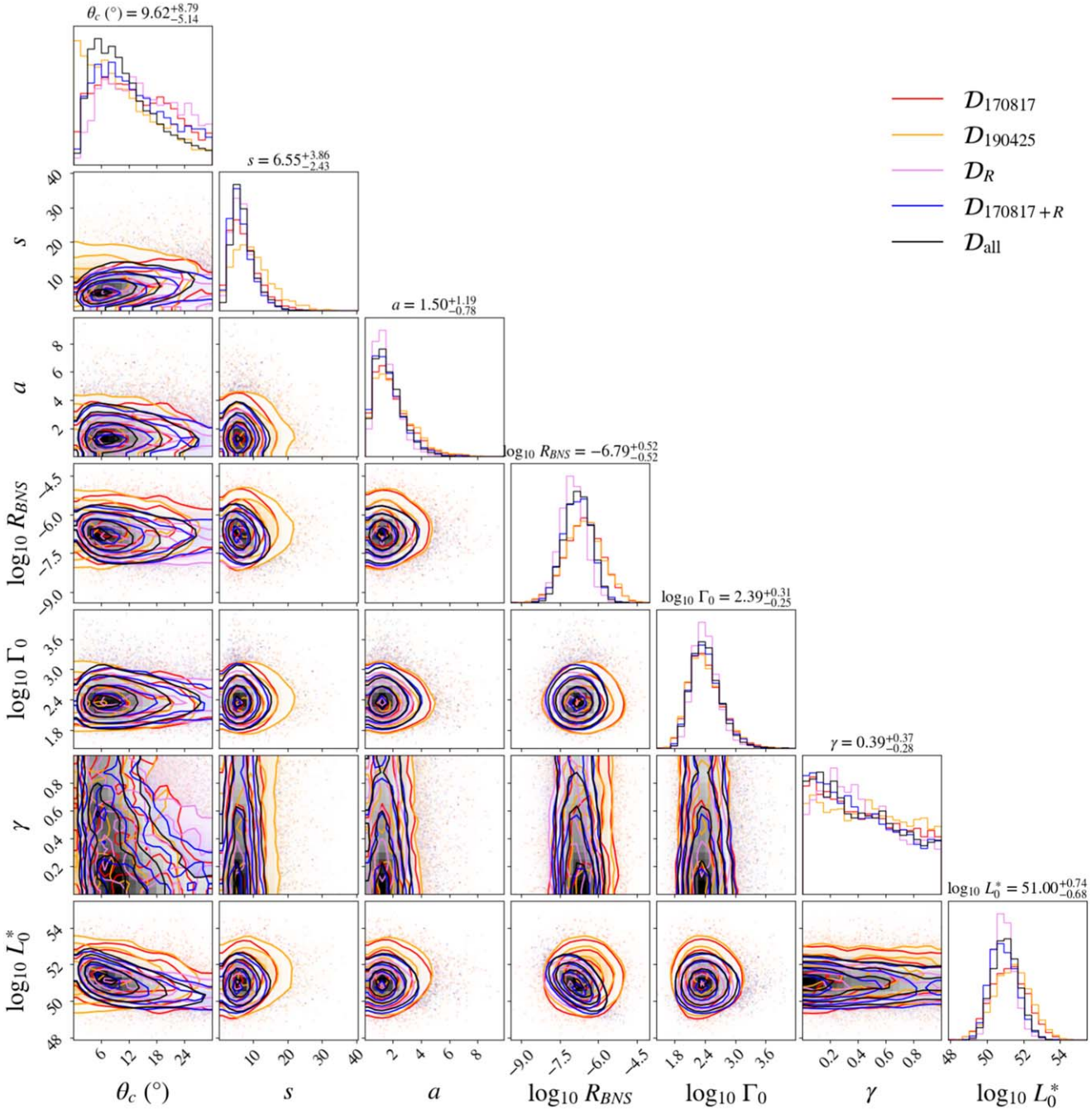

Figure A3. Parameter posterior for all data subsets given the PL jet structure model.

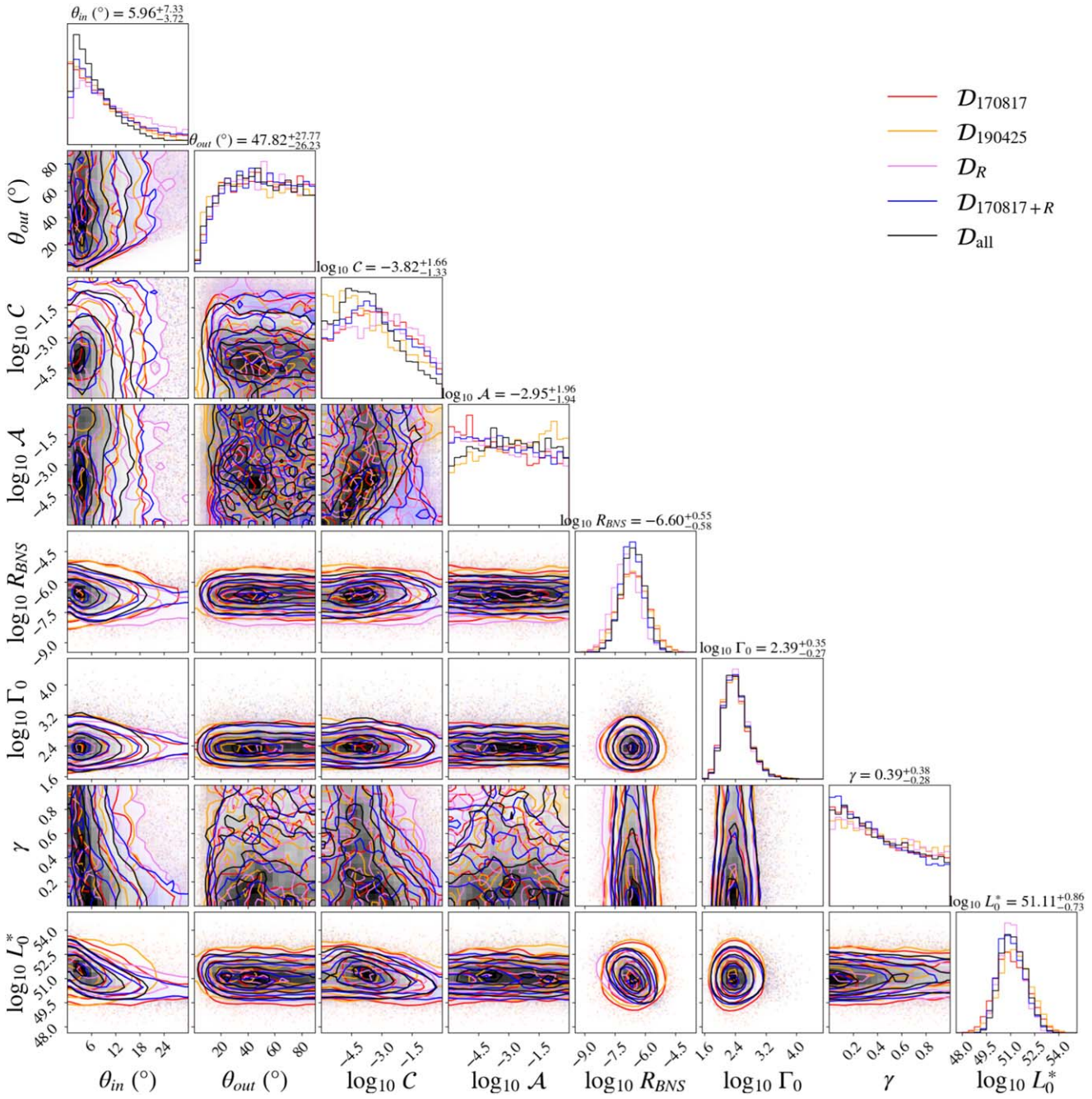

Figure A4. Parameter posterior for all data subsets given the DG jet structure model.

ORCID iDs

Fergus Hayes https://orcid.org/0000-0001-7628-3826
Ik Siong Heng https://orcid.org/0000-0002-1977-0019
Gavin Lamb https://orcid.org/0000-0001-5169-4143
En-Tzu Lin https://orcid.org/0000-0002-0030-8051
John Veitch https://orcid.org/0000-0002-6508-0713
Michael J. Williams https://orcid.org/0000-0003-2198-2974

References

Abbott, B., Abbott, R., Abbott, T., et al. 2019, PhRvX, 9, 011001
Abbott, B., Abbott, R., Abbott, T., et al. 2020a, ApJL, 892, L3
Abbott, B. P., Abbott, R., Abbott, T., et al. 2017a, PhRvL, 119, 161101
Abbott, B. P., Abbott, R., Abbott, T., et al. 2017b, ApJL, 848, L13
Abbott, B. P., Abbott, R., Abbott, T., et al. 2020b, LRR, 23, 1
Abbott, B. P., Abbott, R., Abbott, T. D., et al. 2017c, Natur, 551, 85
Abbott, B. P., Bloemen, S., Canizares, P., et al. 2017d, ApJL, 848, L12
Abbott, R., Abbott, T., Abraham, S., et al. 2020c, ApJL, 913, L7
Abbott, R., Abbott, T., Acernese, F., et al. 2023, PhRvX, 13, 011048
Adam, R., Ade, P. A., Aghanim, N., et al. 2016, A&A, 594, A1
Alexander, K., Margutti, R., Blanchard, P., et al. 2018, ApJL, 863, L18
Amati, L., Frontera, F., Tavani, M., et al. 2002, A&A, 390, 81
Band, D., Matteson, J., Ford, L., et al. 1993, ApJ, 413, 281
Beniamini, P., Granot, J., & Gill, R. 2020, MNRAS, 493, 3521
Beniamini, P., Petropoulou, M., Barniol Duran, R., & Giannios, D. 2019, MNRAS, 483, 840
Biscoveanu, S., Thrane, E., & Vitale, S. 2020, ApJ, 893, 38
Bloom, J. S., Frail, D. A., & Sari, R. 2001, AJ, 121, 2879
Bromberg, O., Tchekhovskoy, A., Gottlieb, O., Nakar, E., & Piran, T. 2018, MNRAS, 475, 2971
Burns, E. 2020, LRR, 23, 1
Cole, S., Norberg, P., Baugh, C. M., et al. 2001, MNRAS, 326, 255

D'Avanzo, P., Campana, S., Salafia, O. S., et al. 2018, A&A, 613, L1
Duffell, P. C., Quataert, E., Kasen, D., & Klion, H. 2018, ApJ, 866, 3
Escorial, A. R., Fong, W.-f., Berger, E., et al. 2022, arXiv:2210.05695
Evans, P., Cenko, S., Kennea, J., et al. 2017, Sci, 358, 1565
Farah, A., Essick, R., Doctor, Z., Fishbach, M., & Holz, D. E. 2020, ApJ, 895, 108
Fernández, J. J., Kobayashi, S., & Lamb, G. P. 2022, MNRAS, 509, 395
Fraija, N., De Colle, F., Veres, P., et al. 2019, ApJ, 871, 123
Galama, T. J., Vreeswijk, P., Van Paradijs, J., et al. 1998, Natur, 395, 670
Ghirlanda, G., Salafia, O. S., Paragi, Z., et al. 2019, Sci, 363, 968
Goldstein, A., Veres, P., Burns, E., et al. 2017, ApJL, 848, L14
Gottlieb, O., Nakar, E., Piran, T., & Hotokezaka, K. 2018, MNRAS, 479, 588
Granot, J., Guetta, D., & Gill, R. 2017, ApJL, 850, L24
Guetta, D., & Piran, T. 2006, A&A, 453, 823
Hayes, F., Heng, I. S., Veitch, J., & Williams, D. 2020, ApJ, 891, 124
Hogg, D. W. 1999, arXiv:astro-ph/9905116
Hopkins, A. M., & Beacom, J. F. 2006, ApJ, 651, 142
Hosseinzadeh, G., Cowperthwaite, P., Gomez, S., et al. 2019, ApJL, 880, L4
Ioka, K., & Nakamura, T. 2019, MNRAS, 487, 4884
Kasliwal, M., Nakar, E., Singer, L., et al. 2017, Sci, 358, 1559
Kathirgamaraju, A., Barniol Duran, R., & Giannios, D. 2018, MNRAS Lett., 473, L121
Kulkarni, S., Frail, D., Wieringa, M., et al. 1998, Natur, 395, 663
Kumar, P., & Granot, J. 2003, ApJ, 591, 1075
Lamb, G. P., Fernández, J. J., Hayes, F., et al. 2021, Univ, 7, 329
Lamb, G. P., & Kobayashi, S. 2017, MNRAS, 472, 4953
Lamb, G. P., & Kobayashi, S. 2018, MNRAS, 478, 733
Lamb, G. P., Levan, A. J., & Tanvir, N. R. 2020, ApJ, 899, 105
Lamb, G. P., Lyman, J. D., Levan, A. J., et al. 2019, ApJL, 870, L15
Lamb, G. P., Nativi, L., Rosswog, S., et al. 2022, Univ, 8, 612
Lazzati, D., Deich, A., Morsony, B. J., & Workman, J. C. 2017a, MNRAS, 471, 1652
Lazzati, D., López-Cámara, D., Cantiello, M., et al. 2017b, ApJL, 848, L6
Lien, A., Sakamoto, T., Barthelmy, S. D., et al. 2016, ApJ, 829, 7
Lien, A., Sakamoto, T., Gehrels, N., et al. 2014, ApJ, 783, 24
Lin, E.-T., Hayes, F., Lamb, G. P., et al. 2021, Univ, 7, 349
Lyman, J., Lamb, G., Levan, A., et al. 2018, NatAs, 2, 751
Margutti, R., Alexander, K., Xie, X., et al. 2018, ApJL, 856, L18
Martin-Carillo, A., Savchenko, V., Ferrigno, C., et al. 2019, GCN Circ., 24169, 1
Mastrogiovanni, S., Duque, R., Chassande-Mottin, E., Daigne, F., & Mochkovitch, R. 2021, A&A, 652, A1
Matsumoto, T., Nakar, E., & Piran, T. 2019, MNRAS, 486, 1563
McCully, C., Hiramatsu, D., Howell, D. A., et al. 2017, ApJL, 848, L32
Mogushi, K., Cavaglià, M., & Siellez, K. 2019, ApJ, 880, 55
Mooley, K., Nakar, E., Hotokezaka, K., et al. 2018, Natur, 554, 207
Nakar, E., & Piran, T. 2016, ApJ, 834, 28
Nakar, E., & Piran, T. 2021, ApJ, 909, 114
Nathanail, A., Gill, R., Porth, O., Fromm, C. M., & Rezzolla, L. 2021, MNRAS, 502, 1843
Petrillo, C. E., Dietz, A., & Cavaglia, M. 2013, ApJ, 767, 140
Poolakkil, S., Preece, R., Fletcher, C., et al. 2021, ApJ, 913, 60
Rossi, E., Lazzati, D., & Rees, M. J. 2002, MNRAS, 332, 945
Rossi, E. M., Lazzati, D., Salmonson, J. D., & Ghisellini, G. 2004, MNRAS, 354, 86
Ruan, J. J., Nynka, M., Haggard, D., Kalogera, V., & Evans, P. 2018, ApJL, 853, L4
Salafia, O. S., Barbieri, C., Ascenzi, S., & Toffano, M. 2020, A&A, 636, A105
Salafia, O. S., Ghirlanda, G., Ascenzi, S., & Ghisellini, G. 2019, A&A, 628, A18
Saleem, M., Resmi, L., Arun, K., & Mohan, S. 2020, ApJ, 891, 130
Sarin, N., Lasky, P. D., Vivanco, F. H., et al. 2022, PhRvD, 105, 083004
Savchenko, V., Ferrigno, C., Kuulkers, E., et al. 2017, ApJL, 848, L15
Takahashi, K., & Ioka, K. 2021, MNRAS, 501, 5746
Tan, W.-W., & Yu, Y.-W. 2020, ApJ, 902, 83
Tanvir, N. R., Levan, A., González-Fernández, C., et al. 2017, ApJL, 848, L27
Troja, E., Piro, L., Ryan, G., et al. 2018a, MNRAS Lett., 478, L18
Troja, E., Piro, L., Van Eerten, H., et al. 2017, Natur, 551, 71
Troja, E., Ryan, G., Piro, L., et al. 2018b, NatCo, 9, 4089
Troja, E., van Eerten, H., Zhang, B., et al. 2020, MNRAS, 498, 5643
Wanderman, D., & Piran, T. 2015, MNRAS, 448, 3026
Williams, D., Clark, J. A., Williamson, A. R., & Heng, I. S. 2018, ApJ, 858, 79
Williams, M. J., Veitch, J., & Messenger, C. 2021, PhRvD, 103, 103006
Zhang, B. 2019, FrPhy, 14, 644021
Zhang, B., Dai, X., Lloyd-Ronning, N. M., & Mészáros, P. 2004, ApJL, 601, L119
Zhang, B., & Meszaros, P. 2002, ApJ, 571, 876